PCCP

Cite this: *Phys. Chem. Chem. Phys.*, 2012, **14**, 15464–15474

www.rsc.org/pccp

PAPER

Structure, spectroscopy and dynamics of layered H_2O and CO_2 ices

Myung Won Lee, Nuria Plattner and Markus Meuwly*

Received 7th June 2012, Accepted 24th September 2012
DOI: 10.1039/c2cp41904a

Molecular dynamics simulations of structural, spectroscopic and dynamical properties of mixed water–carbon dioxide (H_2O–CO_2) ices are discussed over temperature ranges relevant to atmospheric and astrophysical conditions. The simulations employ multipolar force fields to represent electrostatic interactions which are essential for spectroscopic and dynamical investigations. It is found that at the water/CO_2 interface the water surface acts as a template for the CO_2 component. The rotational reorientation times in both bulk phases agree well with experimental observations. A pronounced temperature effect on the CO_2 reorientation time is observed between 100 K and 200 K. At the interface, water reorientation times are nearly twice as long compared to water in the bulk. The spectroscopy of such ices is rich in the far-infrared region of the spectrum and can be related to translational and rotational modes. Furthermore, spectroscopic signatures mediated across the water/CO_2 interface are found in this frequency range (around 440 cm^{-1}). These results will be particularly important for new airborne experiments such as planned for SOFIA.

1 Introduction

Ices exist on the surfaces and in the atmospheres of many planets and their satellites. Major molecular constituents of interstellar ices are H_2O, CO, CH_3OH, CO_2, NH_3, CH_4, HCO, H_2CO, H_2, N_2, O_2, and other small molecules.[1,2] As water is considerably more abundant in interstellar ices than other molecules,[1] H_2O-ices and mixed ices dominated by H_2O are thought to be significant materials of interstellar grains, comets, and many of the outer planetary satellites.[3] The molecular clouds of the Milky Way are considered to have the temperature in the range of 10–20 K and the density in the range of 10^2–10^6 atoms per cm^3.[4]

Ices composed of different molecules play potentially central roles in the origin, evolution, and chemistry of planetary ice surfaces.[5] In order to characterize the chemical processes on planetary surfaces, it is essential to understand the properties of these ices. For remote observations, spectroscopic observables are of particular importance. Infrared observations and laboratory experiments under realistic conditions have contributed significantly to a deeper understanding of interstellar ices and dust particles.[6–13] The constituent molecules comprising interstellar ices can be identified by comparing the observed spectra in the near- and mid-IR range (400–10 000 cm^{-1}) with reference spectra measured in the laboratories.[14–16]

For characterizing not only the different components constituting ices but also the ice structures, it is necessary to establish relationships between observed spectral features and the corresponding ice environment. For ices consisting of H_2O and CO_2, three different types of structures can be envisaged: (a) mixed amorphous ices which are based on random mixtures of H_2O and CO_2 and are only stable at very low temperatures, (b) layered ices which can be formed as a result of subsequent deposition of H_2O and CO_2 and may exist in the stability range of the pure ices of both components, and (c) CO_2 clathrate hydrates[17] which are an ordered and symmetric form of a combined H_2O–CO_2 ice and therefore more stable than random ice mixtures. While the stability ranges and formation conditions differ for these three types of ices, all three ice forms have some spectral features in common due to their chemical composition and interactions. In order to distinguish between the different ice forms, it is necessary to identify spectral features allowing a clear distinction of different ice structures and characterize specific spectral features of each type of ice. While in previous work we have studied the structure–spectroscopy relationships of mixed amorphous ices and CO_2 clathrate hydrates,[18] the aim of this work is to study the layered form of H_2O–CO_2 ices.

A large number of space observatories have been launched into orbit and have greatly enhanced our knowledge about extraterrestrial objects as measurements from Earth's surface have limitations due to the influence of the atmosphere. Modern space telescopes such as the Infrared Space Observatory (ISO), the Spitzer Space Telescope, the Herschel Space Observatory, *etc.* have made it possible to record weak IR signals. There are also airborne observatories, including the Stratospheric Observatory for Infrared Astronomy (SOFIA),[19] which make it possible to avoid the influence of the water vapor

Department of Chemistry, University of Basel, Klingelbergstrasse 80, 4056 Basel, Switzerland

in the atmosphere. The near- and mid-IR wavelength regions contain numerous bands corresponding to molecular vibrations, while the far-IR wavelength region is sensitive to lattice vibrations. The information from the IR spectra is useful in determining the composition and structural characteristics of the ices.[20–23]

While it is possible to investigate such ices remotely by spectroscopic observations, it is difficult to obtain information on structural details. Thus, laboratory experiments are indispensable as the structures of the samples can be probed with various techniques.[6,24–26] Of particular relevance are experiments concerned with layered ices that are grown in a controlled fashion. Otherwise, it is extremely difficult to relate spectroscopic properties with molecular structure because they are amorphous. While mixed H_2O–CO_2 ices exist only at low temperature and/or pressures,[7] less is known about the stability range for layered ices which is likely to be sensitive to the thickness of the layers. For very thick layers, stabilities similar to those of pure H_2O and pure CO_2 ice (dry ice) can be expected, with dry ice being the less stable and therefore the stability limiting component in a binary system. Dry ice exists at higher temperatures and lower pressures than amorphous ices on the basis of random mixtures of H_2O and CO_2 and is therefore found on planetary surfaces, *e.g.* on Mars.[27] CO_2 desorbs from random H_2O–CO_2 mixtures above 100 K whereas dry ice is stable up to about 180 K at low pressures (with a melting point of 195 K at 1 atm pressure). The temperature and pressure range in the present work was therefore chosen by the potential stability range of the ice type we study and by the range of conditions (interstellar, planetary and laboratory) in which this type of ices can be found.

For spectroscopic studies, certain IR active bands are more suitable than others, because the change in the lineshape or frequency can be empirically correlated with the properties of the sample, including chemical composition, concentration or temperature. For example, spectroscopic features such as the near-IR $2\nu_3$ overtone of CO_2 or the water-bending vibration split change shapes in characteristic fashions depending on the amount of CO_2 present.[6,28] It was also found that spectral features of mixed H_2O, CO_2, and CO ices depend on temperature[6,25,29] and are therefore potentially useful to infer physical conditions of the environment. The dangling OH-bond may also be a useful signature as the peak position has been shown to depend upon the type of the adsorbed molecule and temperature.[30–33] The temperatures over which typical laboratory experiments are carried out range from 10 to 180 K.

Computer simulations of ices can give detailed information on such materials that are difficult to access by experiments, thus complementing experimental observations. Ices composed of nonpolar molecules including CO_2 or N_2 usually absorb weakly in the far-infrared region compared with ices containing molecules with O–H bonds. This makes it difficult to study nonpolar molecules mixed with O–H-containing molecules by experiments in this region. Under such circumstances computer simulations are a powerful and convenient means to investigate the details of the system, provided that the intermolecular interactions are described with sufficient accuracy.

In the present work, molecular dynamics (MD) simulations with improved force fields are used to study the structures and infrared spectra of layered H_2O–CO_2 ices. All electrostatic interactions in the H_2O and CO_2 mixture are treated with multipolar force fields, which have provided quantitatively accurate results and detailed insight into spectroscopy–structure relationships.[18,34–37] Depending on the conditions of the ice formation, interstellar and planetary ice mixtures can exist in amorphous or layered forms, with varying layer compositions. Based on the structural and spectroscopic features of different ice layers and their proximity to the H_2O/CO_2 interface, properties of layered ices are discussed more generally. Of particular interest is the possibility to correlate spectroscopic features with structural and dynamical characteristics which will be of practical interest in analyzing laboratory spectra or those recorded from satellite missions.

2 Computational methods

All molecular dynamics (MD) simulations were carried out using the CHARMM program[38] with provisions for calculating multipolar interactions.[37] The simulations employed periodic boundary conditions in the *NPT* ensemble using a Nosé–Hoover thermostat[39,40] at temperatures between 20 and 200 K (20, 50, 100, 150 and 200 K) and the time step in all simulations was 0.4 fs to account for the flexible water molecules (see below). Nonbonded interactions (electrostatic interactions and Lennard-Jones potentials) were included completely when the interatomic distances were less than 10 Å, and switched between 10 and 12 Å.

The preparation of the mixed H_2O–CO_2 layer is shown in Fig. 1. It was set up as follows: an initially hexagonal H_2O structure was brought into contact with CO_2 in its dry ice structure.[41] The box has dimensions $35 \times 66 \times 28$ Å^3 and contains 1024 H_2O molecules and 672 CO_2 molecules (5088 atoms in total). The initial layered structure was minimized using the steepest descent method for 100 steps, heated to the desired temperature (20–200 K) in 0.2–1.6 ps, and then equilibrated for about 120–160 ps before the production run of 100 ps. Five independent 100 ps trajectories were generated at each temperature. As pointed out in the "Introduction", simulations at lower temperatures are more relevant in an astrophysical context, whereas those at higher temperatures (150 and 200 K) are relevant because the results can be extrapolated to validate them vis-a-vis experiments carried out at even higher temperatures. Furthermore, it is expected that layered H_2O–CO_2 ices are stable over a wider temperature range and future experiments on them can be compared with the results from the present work.

For the water molecules, a flexible water model based on the parametrization by Kumagai, Kawamura, and Yokokawa (KKY)[42] was used. All parameters were the original KKY potential parameters[42] (D = 75.0 kcal mol^{-1}, β = 2.74 Å^{-1}, r_0 = 0.82 Å, f_k = 1.1 × 10^{-11} J, r_m = 1.40 Å, and g_r = 7.0 Å^{-1}) except for the bending force constant, f_k, which was decreased to 1.7 × 10^{-19} J (~24 kcal mol^{-1}) to reproduce the correct bending frequency of H_2O. This has been found necessary in previous work.[18,43,44] For carbon dioxide, the parameters used in the previous work were adopted without modifications,[18] where K_b = 1019 kcal mol^{-1} Å^{-2} and b_0 = 1.16 Å for C–O stretching and K_θ = 55.56 kcal mol^{-1} rad^{-2} and

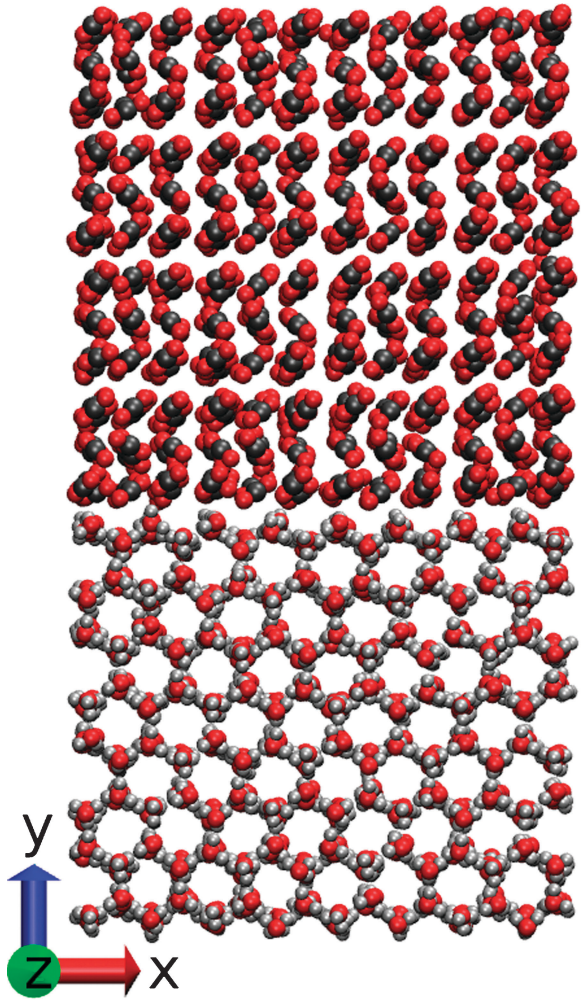

Fig. 1 Structure of the layered CO_2–H_2O ice system used in this work. The CO_2 layers shown in the upper part are placed in contact with the H_2O layers in the lower part. The CO_2 layers have the dry ice structure and the H_2O layers have the hexagonal ice structure.

$\theta_0 = 180^\circ$ for the O–C–O bending. The parameters give harmonic frequencies of 1598, 3684, and 3719 cm^{-1} for H_2O (*vs.* 1595, 3657, and 3756 cm^{-1} from experiment[45]) and 668, 1226, and 2346 cm^{-1} for CO_2 (*vs.* 667, 1333, and 2349 cm^{-1} from experiment[46]).

For H_2O and CO_2 molecules, fixed multipole moments up to quadrupole obtained from the MP2 level calculations with D95 basis set were adopted from previous work.[18] This is referred to parameter set MTP(I). These multipoles gave relative intensities for CO_2 modes much smaller than those observed in experiments.[28] Nevertheless, the positions of the CO_2 peaks could be reproduced correctly. For comparison, a reparametrization of the H_2O and CO_2 MTPs from B3LYP/aug-cc-pVQZ calculations was carried out using Gaussian 03,[47] which leads to mutipolar model MTP(II). All multipoles used in this work are given in Table 1. It was found (see below) that MTP(II) gave more realistic relative IR intensities for the asymmetric stretching and bending modes of CO_2, while the peak positions were virtually unchanged compared to those from MTP(I).

Orientational probability functions of the molecules can help to more globally describe the morphology of a surface.

Table 1 Multipole moments of H_2O and CO_2 used in this work. MP2/D95 or B3LYP/aug-cc-pVQZ calculations were used to produce parameters. Each multipole component is static, *i.e.*, it does not depend on the geometry of the molecule. In the multipole component Q_u, u represents angular momentum labels (00, 10, 11c, 11s, 20, 21c, 21s, 22c, and 22s). The units of Q_u are given in parentheses in the table. Only nonzero components are shown. To distinguish different parameter sets, they are labeled MTP(I) and MTP(II)

			MTP(I) MP2/D95	MTP(II) B3LYP/aug-cc-pVQZ
H_2O	Q_{00}^{O}	(e)	−0.280016	−0.382464
	Q_{10}^{O}	(ea_0)	−0.418741	−0.309597
	Q_{20}^{O}	(ea_0^2)	0.028448	0.129376
	Q_{22c}^{O}	(ea_0^2)	−1.687540	−1.347569
	Q_{00}^{H}	(e)	0.140008	0.191232
CO_2	Q_{00}^{C}	(e)	0.031976	0.431038
	Q_{20}^{C}	(ea_0^2)	0.509873	0.563097
	Q_{00}^{O}	(e)	−0.015988	−0.215519
	Q_{10}^{O}	(ea_0)	−0.673825	−0.390068
	Q_{20}^{O}	(ea_0^2)	0.848992	0.797539

For this, the angular orientations of the molecules of interest are required. For CO_2 the angle $\theta \in (0, 90^\circ)$ is measured between the y-axis (perpendicular to the H_2O/CO_2 interface, see Fig. 1) and the O–O vector of the CO_2 molecule whereas $\phi \in (-180^\circ, 180^\circ)$ is defined as the angle between the z-axis and the projection of the O–O vector onto the interface plane (xz-plane). While one vector connecting two O atoms is sufficient to represent the molecular orientation of a CO_2 molecule, two vectors, $\boldsymbol{\nu}_1$ and $\boldsymbol{\nu}_2$, are necessary to define the direction of a H_2O molecule. $\boldsymbol{\nu}_1$ bisects the H–O–H angle and $\boldsymbol{\nu}_2$ is perpendicular to the plane of the water molecule, as shown in Fig. 2a. The direction of each vector was associated with θ and ϕ angles, as for CO_2. The angles θ_1 and ϕ_1 are associated with $\boldsymbol{\nu}_1$, whereas θ_2 and ϕ_2 with $\boldsymbol{\nu}_2$. The vector $\boldsymbol{\nu}_1$ and the associated angles θ_1 and ϕ_1 are shown in Fig. 2b. While θ_1 ranges from 0 to 180°, θ_2 ranges from 0 to 90° due to the symmetry of the molecule. Both ϕ_1 and ϕ_2 range from −180° to 180°.

Infrared (IR) spectra are calculated from the Fourier transform of the dipole moment autocorrelation function, $C(t) = \langle \mu(0) \cdot \mu(t) \rangle$ which is accumulated over 2^n time origins, where n is an integer such that 2^n corresponds to between 1/3 and 1/2

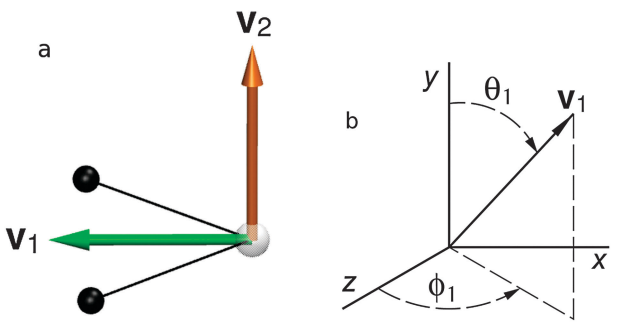

Fig. 2 (a) The two vectors $\boldsymbol{\nu}_1$ and $\boldsymbol{\nu}_2$ used to represent the orientation of a water molecule. The two hydrogen atoms are shown in black spheres and the oxygen atom as a gray transparent sphere. $\boldsymbol{\nu}_1$ bisects H–O–H angle and $\boldsymbol{\nu}_2$ is perpendicular to the molecular plane. (b) The angles θ_1 and ϕ_1 associated with the vector $\boldsymbol{\nu}_1$. θ_1 is the angle between $\boldsymbol{\nu}_1$ and the y-axis, and ϕ_1 is the angle between the projection of $\boldsymbol{\nu}_1$ onto xz-plane and the z-axis. θ_2 and ϕ_2 are computed similarly to $\boldsymbol{\nu}_2$.

of the trajectory, with the time origins separated by 0.8 fs. $\hat{C}(\omega)$, which is the Fourier transform of $C(t)$, is computed using a Fast Fourier Transform (FFT) with a Blackman filter for the reduction of noise.[48] The final infrared absorption spectrum $A(\omega)$ is then calculated from

$$A(\omega) \propto \omega \{1 - \exp[-\hbar\omega/(k_B T)]\}\hat{C}(\omega), \quad (1)$$

where k_B is the Boltzmann constant and T is the absolute temperature in Kelvin. Layer-specific IR spectra were also obtained by correlating total dipole moments from one particular H_2O or CO_2 layer.

Rotational correlation times τ_l for the CO_2 and H_2O molecules were calculated from[49]

$$C_l(t) = \langle P_l(\boldsymbol{u}(0)\cdot\boldsymbol{u}(t))\rangle, \quad (2)$$

where $C_l(t)$ is the rotational correlation function, P_l is the Legendre polynomial of order l, and $\boldsymbol{u}(t)$ is a unit vector representing molecular orientations at time t. For CO_2, the unit vector points along the molecular axis which is computed from the coordinates of the two oxygen atoms. For H_2O, several different unit vectors can be considered. Four types of unit vectors were used in the calculation of the rotational correlation functions: the H–H axis ($\boldsymbol{u}_{HH}$), the O–H axis ($\boldsymbol{u}_{OH}$), the molecular dipole ($\boldsymbol{u}_\mu$), and the normal to the molecular plane ($\boldsymbol{u}_\perp$).[50] In the present work P_2 was used to compare with NMR experiments.[51] The rotational correlation time τ_l can be computed from[49]

$$\tau_l = \int_0^\infty C_l(t)\mathrm{d}t. \quad (3)$$

Alternatively, if $C_l(t)$ has a single exponential decay $C_l(t) \approx e^{-l(l+1)D_R t}$ – as was the case in the present work – the rotational correlation time can be obtained from $\tau_l \approx 1/[l(l+1)D_R]$. Therefore, $C_2(t)$ was fitted to an exponential function $ae^{-t/\tau_2} + c$ to compute τ_2. Layer-specific reorientation times are averages over all CO_2 or H_2O molecules in one selected layer.

3 Results and discussion

In the following, structural features are discussed first. Next, results on the IR spectroscopy are presented and finally rotational reorientation times are analyzed. Comparing experiments and simulations we find that (a) the low-frequency (translational) spectrum in hexagonal ice Ih is quite well captured, (b) the librational modes are correctly described, (c) the width of the water-stretching modes is too narrow in the simulation and is not sufficiently redshifted compared to the gas-phase experiments, and (d) the far-IR CO_2 modes are correctly positioned.

Structural features of the layers: the radial distribution functions (RDFs) for CO_2 and H_2O are reported in Fig. 3. They show the influence of the local environment on the structure of each molecular species. Since the particular environment of the molecules is layer-dependent, it is expected that the contribution of different layers to the IR spectra reflects this structural change through variations in frequency shifts and intensities, especially in the low-frequency region associated with lattice vibrations.

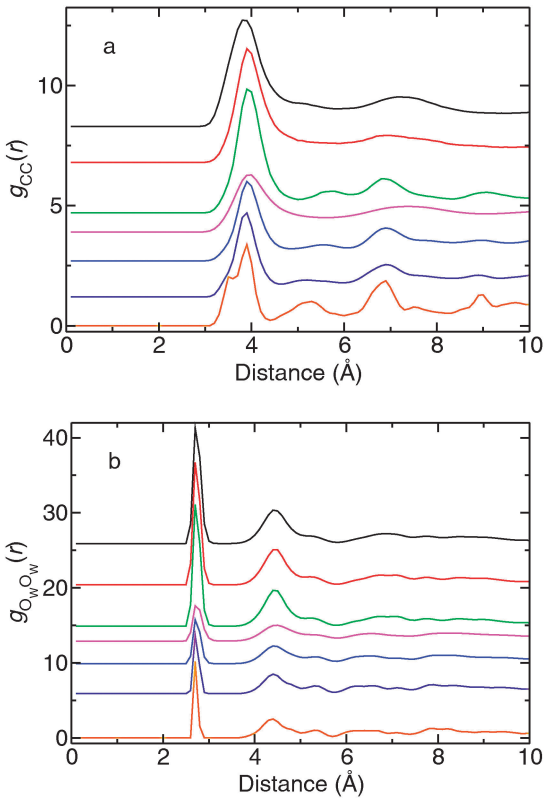

Fig. 3 Radial distribution functions (RDFs) of the C atoms of the CO_2 molecules (upper panel) and of the O atoms of the H_2O molecules (lower panel) for the 1st (black), 2nd (red), and 3rd (green) layers from the interface at 100 K and for all the layers at 150 K (magenta), 100 K (blue), 50 K (violet), and 20 K (orange). The RDFs corresponding to interface layers differ from the overall RDFs.

For the RDFs of CO_2 it is found that $g_{CC}(r)$ displays a secondary maximum between 6 and 8 Å, which is broad and located above 7 Å for the first CO_2 layer and becomes narrower and shifts below 7 Å for the CO_2 molecules away from the 1st layer. This indicates that the local structure of the CO_2 molecules in the 1st layer is distorted from its bulk arrangement through interactions with the neighboring water molecules and that the structure of the CO_2 molecules a few layers away from the interface would be similar to that of bulk CO_2. We also note that the RDFs are more structured at lower temperatures and become less pronounced at higher temperatures, which is due to increased motion at higher temperatures. For the water-RDFs most of the features in the bulk- and the 3rd layer at 100 K are also found for water molecules in the 1st layer. Thus, the water molecules are less affected by the presence of the CO_2 molecules than *vice versa*. In other words, the water surface appears to be a template for the CO_2 molecules. It can be observed in the RDFs of CO_2 at 100 K that the peak just below 7 Å for overall CO_2 moves slightly above 7 Å for the 1st layer CO_2, which can be related to the lattice constant of hexagonal ice $c = 7.32$ Å, as the CO_2/H_2O interface is parallel to the c-axis of the hexagonal ice in our simulations.

A more quantitative comparison of the different layers is provided by orientational probability functions (OPFs) of the molecules in particular layers. The OPFs were computed from the trajectories of the layered H_2O–CO_2 system at 100 K.

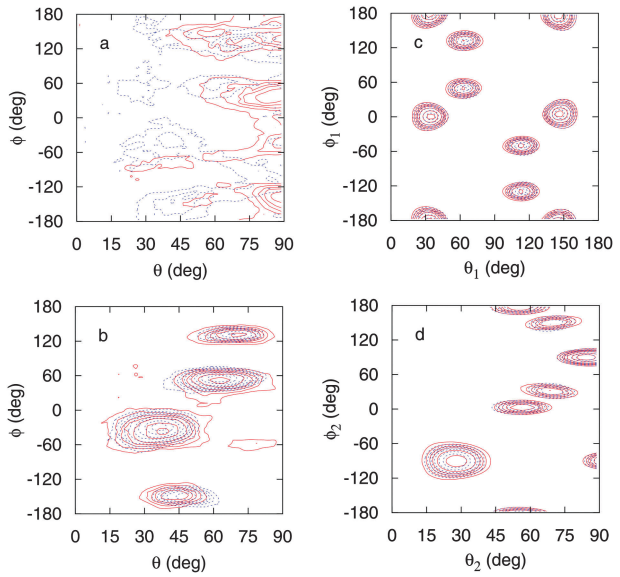

Fig. 4 (a) and (b) The orientational probability functions (OPFs) of the CO_2 molecules. The OPFs from the 1st (red) and 2nd (blue) CO_2 layers are shown in (a) and those from the 3rd (red) and 4th (blue) layers in (b). (c) and (d) The OPFs of the H_2O molecules. The OPFs for the bisector of H–O–H angle (ν_1) are shown in (c) and those of the normal vector to the molecular plane (ν_2) in (d). The OPFs from the 1st layer are shown in red and the OPFs from the 3rd layer in blue.

OPFs for the CO_2 molecules in the 1st to 4th layers are reported in Fig. 4a and b and show several characteristic maxima. In Fig. 4a and b the difference between CO_2 layers is clearly visible. In particular, the 1st and 2nd layers are somewhat disordered compared to layers 3 and 4 which are considerably more ordered. It is also apparent that the CO_2 molecules in the 1st layer have maxima in the OPFs that are different from those of other layers due to the neighboring water molecules. For water in the 1st and 3rd layers the OPFs are displayed in Fig. 4c and d. All the layers investigated (from the 1st to the 4th) show maxima at the same positions which emphasizes the well-defined positions of the water molecules within a lattice. Furthermore, it is interesting to observe that the maxima in the OPFs of CO_2 in the first layer (red trace in Fig. 4a) appear rather at the maxima of the water lattice (Fig. 4d) than at those from the CO_2 lattice in Fig. 4b. This is most clearly seen for the peak at $(\theta, \phi) = (30^\circ, -90^\circ)$ for first-layer CO_2 which shifts to $(\theta, \phi) = (40^\circ, -30^\circ)$ for CO_2 in subsequent layers. The water lattice has a pronounced peak at $(\theta_2, \phi_2) = (30^\circ, -90^\circ)$ which underlines a templating effect.

The distribution of the bond angles θ of H_2O and CO_2 during the MD simulations (not shown) further indicates that the water molecules at the interface strongly affect the neighboring CO_2 molecules. The typical widths of the bond angle distributions are $\approx 5^\circ$ for H_2O in all layers compared to gas-phase water molecules, irrespective of the layer they are in. In contrast to that, the bond angles of the first- and second-layer CO_2 molecules vary by up to 5° and 2°, respectively. This is a larger variation than in bulk-CO_2 which was found to be 1° and further strengthens the notion that water strongly influences CO_2-layers close to the interface.

IR spectra in high-frequency region: the IR spectra calculated from the MD simulations with MTP(I) for the layered

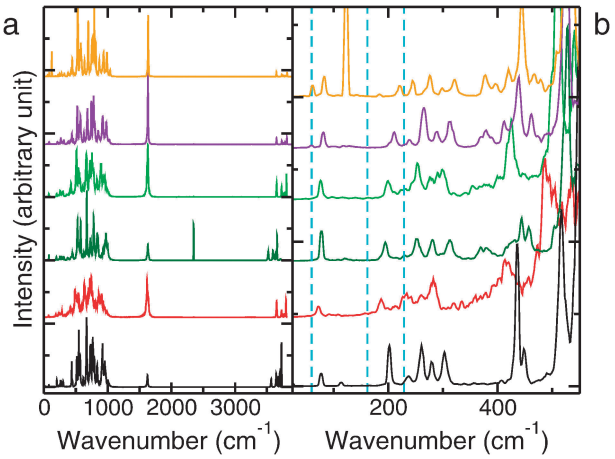

Fig. 5 Calculated IR spectra of the layered H_2O–CO_2 and pure hexagonal ice in the entire range are shown in (a) and in the far-IR region in (b). Spectra of the layered ice at 20, 50, 100, and 150 K computed with MTP(I) are shown in orange, violet, green, and red, respectively. The spectrum of the layered ice at 100 K computed with MTP(II) is shown in dark green. For comparison, the IR spectrum of pure hexagonal ice at 100 K is shown in black. In (b), the experimental peak positions of hexagonal ice are indicated by dashed vertical lines (cyan).

H_2O–CO_2 ices at 20, 50, 100, and 150 K are reported in Fig. 5. For the following, it is important to mention that the IR spectra are computed from the dipole–dipole autocorrelation function and therefore yield intensities that can be compared for the H_2O and CO_2 signals. Absolute intensities could be computed by taking into account suitable conversion factors.[52] The spectra computed at different temperatures in Fig. 5 show that fine features at low temperature disappear at high temperature as the features broaden. This is in line with what is observed in the RDFs at different temperatures. For comparison, the IR spectrum of pure hexagonal ice (Ih) at 100 K is also shown.

Three different IR spectra of the layered system have been computed: (1) from H_2O molecules only (blue traces in Fig. 6),

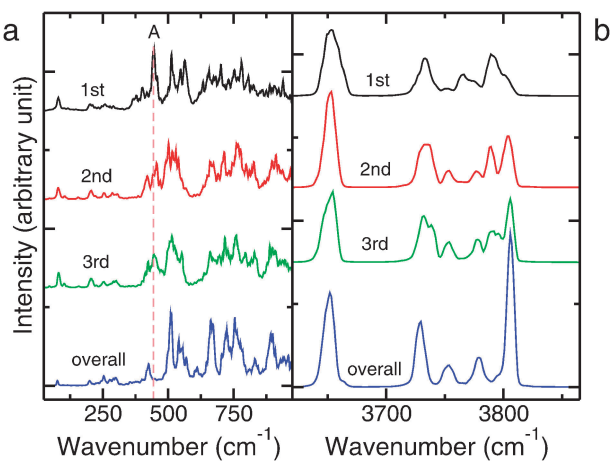

Fig. 6 Layer-specific IR spectra for water in H_2O–CO_2 at 100 K in the (a) low- and (b) high-frequency region. Spectra are reported for water molecules in the 1st (black), 2nd (red), and 3rd (green) layer away from the interface and from all H_2O molecules (blue). In (a), a vertical dashed line is shown at 444 cm^{-1} to guide the eye.

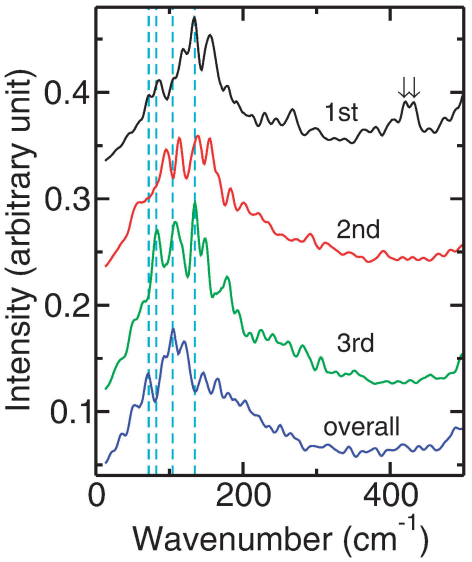

Fig. 7 Layer-specific far-IR spectra for CO_2 in H_2O–CO_2 at 100 K. The spectra shown are for CO_2 molecules in the 1st (black), 2nd (red), and 3rd (green) layer away from the H_2O/CO_2 interface and from all CO_2 molecules (blue). The vertical dashed lines in cyan color are added in the region around 100 cm^{-1} to guide the eye. Two downward arrows are shown around 421 and 432 cm^{-1} (see the text).

(2) from CO_2 molecules only (blue trace in Fig. 7 in the low-frequency region, high-frequency region not shown), and (3) including all molecules (green traces in Fig. 5). The spectra of (1) and (3) almost coincide except for two small peaks which correspond to CO_2 (ν_2 and ν_3) modes. Conversely, spectrum (2) is quite different, showing two major peaks corresponding to the CO_2 asymmetric stretching (ν_3) and bending (ν_2) vibration, as well as some others in the far-IR region. As each spectrum is separately normalized, features of CO_2 which are very weak in (3) are greatly amplified in (2). It is clear that the spectra computed from MD simulations are dominated by the water signal.

The IR spectra of the layered system at 100 K were also computed with MTP(II) and are reported in Fig. 5. In this model the charges on the C- and O-atoms of CO_2 are larger in magnitude and accordingly the intensities of the CO_2 bending and asymmetric stretching modes are somewhat increased in the IR spectrum of the mixed system. However, the computed spectrum of the overall system is still mainly composed of the signal from H_2O molecules. The bands in the far-IR region are almost coincident whereas above $\approx$250 cm^{-1} bands appear at different frequencies. This suggests that modifications in the force field affect both, relative intensities and actual frequencies.

In the O–H stretching region the computed modes of H_2O show a well-resolved spectrum including 5 distinct peaks for hexagonal ice at 100 K: 3567, 3645, 3669, 3701, and 3728 cm^{-1}. In contrast to that, the experimentally observed OH-stretching appears as one broad band in the range of 3100–3400 cm^{-1} in hexagonal ice (Ih).[53] The gas-phase modes of H_2O observed from IR are at 1595, 3657 (or 3655 from Raman) and 3756 cm^{-1} for the bending, symmetric and asymmetric stretching modes, respectively.[45,54] This compares with gas-phase frequencies of 1598, 3697, and 3733 cm^{-1} from simulations of free H_2O at 100 K with the parameters used in this work. Experimentally, liquid H_2O at 300 K shows one broad absorption band extending from 3200 to 3600 cm^{-1}.[55] This corresponds to redshifts of the spectrum by 100 to 500 cm^{-1} compared to the gas phase. The experimentally observed redshift in the condensed-phase spectrum relative to that in the gas phase is known to be difficult to reproduce in computer simulations.[56] It is possible that more extensive averaging will broaden the computed spectrum which, however, will not improve the situation for the relative redshift in going from the gas to the condensed phase. The assignments of the high-frequency peaks (ν > 3000 cm^{-1}) in terms of OH-stretches are quite clear ("free" *vs.* "H-bridged" OH) whereas details are delicate. The lower frequencies of water stretching modes in our computed IR spectra of ice compared with frequencies of free H_2O reflect the hydrogen bonding in the system. A more detailed discussion is given in the section *Power spectra* below. For the H_2O bending mode, a peak is found at 1625 cm^{-1} from the simulation of pure H_2O at 100 K. The blueshift of the bending mode in the condensed phase compared with the gas-phase water is also observed in the experimental IR spectra[57] and is attributed to the hydrogen bonding. We note in Fig. 5a that the IR spectrum computed at 100 K with MTP(II) shows a redshift of the OH stretching region, compared with the gas-phase frequencies, which is in accord with the experiment, while the magnitude of redshift from the simulation is not as large as that from the experiment. This is in contrast with the simulations with MTP(I), which do not show appreciable redshift. However, broadening of the spectra in the ice is not found in the simulations.

The CO_2 antisymmetric stretching mode appears as one single peak at around 2349 cm^{-1} in the computed IR spectra of the layered H_2O–CO_2 ice and is quite independent of temperature between 20 and 150 K. The CO_2 bending mode behaves similarly to the antisymmetric stretching. The combination modes of CO_2 for $\nu_1 + \nu_3$ and $2\nu_2 + \nu_3$ are observed in the experimental IR spectra of pure CO_2 or 5 : 1 mixture of H_2O–CO_2 at around 3700 and 3600 cm^{-1}.[28] These combination bands are not discernible in the computed IR spectrum of pure CO_2 ice. For the layered H_2O–CO_2 ice, strong water lines are found in the 3720–3820 cm^{-1} region and it is difficult to discern them from the CO_2-combination bands. To facilitate the analysis, the IR spectrum has been computed using the dipole moment contribution only from the CO_2 molecules. In this IR spectrum, we observe weak bands at around 3750 cm^{-1}. The CO_2 power spectra for the ν_1 and ν_3 modes from the simulations of the layered H_2O–CO_2 ice display small peaks at around 3659 cm^{-1} and in the range of 3730–3800 cm^{-1} for ν_1, which may be related to the combination bands. This is consistent with previous *ab initio* molecular dynamics simulations on water and ice which have shown to give correct infrared spectra of water and ice, including the combination band.[58] It has been shown that couplings between different degrees of freedom can be revealed by using the power spectra.[59]

IR spectra in low-frequency region: below 250 cm^{-1} and at 100 K, the computed spectra for pure hexagonal ice show discrete bands at 77 and 235 cm^{-1} and weak signals at 114 and 166 cm^{-1}. Experiments in the far-IR region on pure hexagonal ice between 100 and 500 cm^{-1} and at temperatures 13 and 155 K yield peaks at 162 and 229 cm^{-1}.[60,61] Raman

spectroscopy even found a lower-frequency peak at around 60 cm^{-1} at 257 and 61.5 K, respectively.[62,63] All these bands are assigned to the translational motion of the water molecules based upon the power spectrum, which is described further below. The assignment has been made previously from the experiments in the far-IR region, where the IR frequency ratio for H_2O and D_2O ices is close to $\sqrt{20/18} \approx 1.05$, which confirms the assignment to the translational motion of the water molecules.[64] Inelastic neutron scattering experiments of water ice Ih at 20 K find broader features in the low frequency region around 40–100 cm^{-1}, 120–180 cm^{-1}, and 195–235 cm^{-1}, respectively.[65] Thus, the computed spectra are able to capture the number of bands and approximately reproduce their position. However, depending on the technique used, experiments also find slightly different frequencies for the excitations in the far-IR in ice Ih. We note that in the simulations, too, the peaks are somewhat blueshifted when the temperature is reduced from 100 to 20 K, *e.g.*, from 77 to 82 cm^{-1}, from 114 to 121 cm^{-1}, and from 235 to 250 cm^{-1}. One noteworthy feature appears in the mixed ice around 120 cm^{-1} at 20 K (top trace in Fig. 5b). This signal has increased intensity relative to the neighboring peaks compared to spectra at 50 K or 100 K. The peak at 120 cm^{-1} is also weakly present in hexagonal ice. This and additional simulations with artificially increased masses on the CO_2 molecules suggest that the signal is due to water molecules at the interface. Power spectra support the assignment to water-translational modes. The enhanced intensity may originate from a dynamically arrested state which is liberated at higher temperatures and does not lead to a spectroscopic signal. This is further supported by simulations at 20 K which started from structures at 50 K and lead to the same spectral feature at 120 cm^{-1}.

Higher in frequency are the water librational modes, ν_R, which appear in the range between 380 and 1050 cm^{-1} from the simulations as shown in Fig. 5. This compares with the experimental bands in ice Ih at 100 K, which are located between 525 and 1040 cm^{-1}.[66] Thus, good agreement is found for the librational bands. The experimental IR spectrum shows again broad librational bands compared with the computed spectra, which are composed of many narrow peaks in this range. More conformational averaging is expected to broaden these spectra because they consist of many individual and narrow spectral features characteristic of the different conformations sampled. If the dipole moment of the entire system is used for calculating the IR spectra from the MD simulations, the peaks due to CO_2 are very weak. For that reason, $\mu_{CO_2}(t)$ was separately analyzed. In the far-IR region, peaks are found at 71 and 120 cm^{-1} from the simulations at 100 K (see Fig. 7) compared with 68 and 114 cm^{-1} from experiments on pure CO_2 at 77 K.[67] This serves as an additional validation of the approach used here. Similarly to water, we note that the experimental far-IR spectrum of CO_2 shows two broader peaks in the range of 40–160 cm^{-1}, while there are more narrower peaks for the spectra from simulations. While the IR bandshapes from simulations are somewhat different from those from experiments, the bands appear around the same range.

Layer-specific spectra of H_2O: while some experimental techniques, such as sum frequency generation (SFG) spectroscopy,[68] are sensitive to one or a few monolayers of a surface, it is in general difficult to obtain layer-specific information from experiment. This is one of the advantages of computer simulations as they allow us to specifically analyze subsystems and therefore complement experimental investigations. The IR spectra from the 1st, 2nd, and 3rd layers of H_2O away from the interface are shown in Fig. 6, together with the spectrum from all H_2O layers. The low-frequency region ($\nu < 1000$ cm^{-1}) for the H_2O layers is shown in Fig. 6a and the high-frequency region ($\nu > 3600$ cm^{-1}) in Fig. 6b. Some peaks are more pronounced in certain layer-specific IR spectra. For example, a peak at around 444 cm^{-1} (label A in Fig. 6a), which corresponds to a water libration mode according to our assignment (see below), is prominent in the spectrum of the 1st H_2O layer. This peak is somewhat weaker in the spectra of the 2nd and 3rd layers, and very weak in the overall spectrum. One possible interpretation of this peak is that it corresponds to a less restricted rotational motion in a particular direction for water molecules directly at the interface due to the presence of CO_2, and becomes more hindered for subsequent layers due to hydrogen bonding between water molecules for subsequent layers.

In the high-frequency region, the peak at around 3806 cm^{-1} is very strong in the overall spectrum, while it is basically absent in the 1st-layer spectrum. To help the assignment, we obtained the power spectra of H_2O molecules in the layered H_2O–CO_2 ice. The power spectra for the symmetric and asymmetric stretching modes have been computed in addition to that for the bending mode. The peak at around 3654 cm^{-1} can be found in the power spectrum for the symmetric stretching mode, which corresponds to the peak at around 3652 cm^{-1} in the overall IR spectrum. Power spectra for the asymmetric stretching mode find bands between 3710 and 3815 cm^{-1} which can be correlated with the peaks at around 3729, 3753, 3779, and 3806 cm^{-1} in the overall IR spectrum.

Layer-specific spectra of CO_2: for the high-frequency region, the bending and asymmetric stretching modes are prominent (not shown in figure) and their positions vary little, irrespective of the layers, while the intensity ratios vary depending on the layers. The far-IR spectra from all CO_2 molecules and those of the 1st, 2nd, and 3rd layers away from the interface are shown in Fig. 7. Peaks in the 50–200 cm^{-1} range blueshift for molecules in layers close to the H_2O/CO_2 interface. We note the double peak at around 425 cm^{-1} in the IR spectrum from the 1st layer (labeled with arrows). To assign this peak, the translational and rotational power spectra of CO_2 have been obtained for the 1st, 2nd, and 3rd layers from the interface. The translational power spectrum along the x-direction supports the assignment of this peak to the translational motion of CO_2 in the x-direction. Together with the analysis of the water spectra in this frequency range it suggests that this motion is coupled to the first few water layers at the interface (see peak A in Fig. 6a).

Power spectra: to help assign additional features in the IR spectrum, the power spectrum was obtained for pure hexagonal ice at 100 K from the velocity–velocity autocorrelation function of the oxygen atoms (see Fig. 8). Upon comparing the IR and power spectra of pure H_2O it is found that the IR peaks below 400 cm^{-1} also appear in the power spectrum, which indicates that these peaks correspond to the translational motion of the water molecules. This is also confirmed by the isotope effects mentioned above. Above 500 cm^{-1} no peaks are found in the

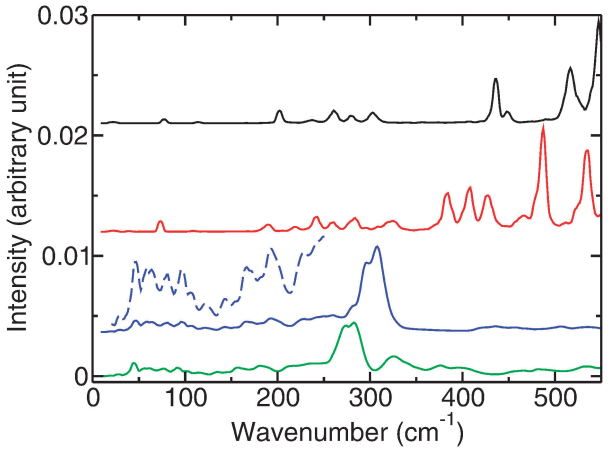

Fig. 8 Computed far-IR spectra of pure hexagonal ice of H_2O (black) and D_2O (red) at 100 K are shown, together with the power spectra obtained from the oxygen atoms of H_2O (blue) and D_2O (green). For clarity, part of the power spectrum of H_2O is enlarged and displayed in blue dashed line.

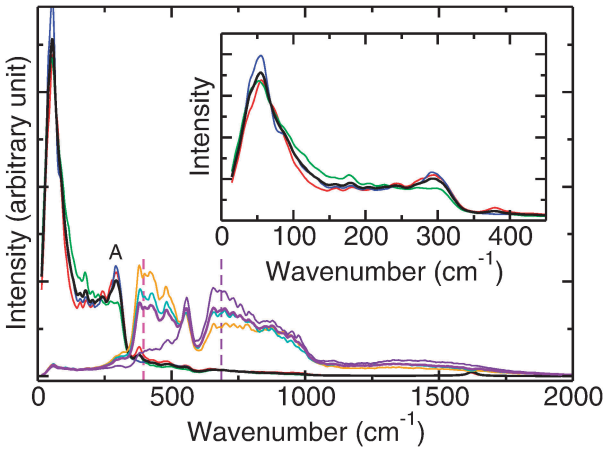

Fig. 9 Power spectra for the translational (black) and rotational (violet) motions of the first-layer H_2O molecules from the H_2O/CO_2 interface averaged over all three directions. The *x*-, *y*-, and *z*-components of the translation are shown in red, green, and blue, respectively, and the *x*-, *y*-, and *z*-components of the rotation are shown in orange, turquoise, and indigo, respectively. The vertical dashed lines in magenta at 396 cm^{-1} and in violet at 686 cm^{-1} indicate the experimental positions of L_1 and L_2 bands at 273 K, respectively. The inset shows enlarged power spectra for the translation in the FIR region using the same color scheme.

translational power spectrum. Therefore, the signal in the IR spectrum in this range is assigned to the water librational modes. The power spectrum of H_2O is structured with signals between 50 and 100 cm^{-1}, at 167, and 229 cm^{-1}, which can be correlated with the experimental frequencies of 60, 162, and 229 cm^{-1} mentioned above.

Power spectra corresponding to the water translation and libration were also calculated for the water molecules in the first layer from the H_2O/CO_2 interface. To this end, Fourier transforms of the autocorrelation functions were computed from the space-fixed *x*-, *y*-, and *z*-coordinates of the water oxygen atoms for the translational motion and from the rotational angles of the water molecules in the molecule-fixed *x*-, *y*-, and *z*-directions for the rotational motion. The spectra thus obtained were averaged over *x*-, *y*-, and *z*-directions and are displayed in Fig. 9. The power spectrum from the position of oxygen atoms shows broad bands between 40 and 340 cm^{-1}, indicating that this range corresponds to the translational motion of the water molecules, while the spectrum from the rotational angles shows a broad band in the 380–560 cm^{-1} region, supporting the interpretation of the IR band between 500 and 550 cm^{-1} as water libration. Two librational modes are observed experimentally, the L_1 mode at around 396 cm^{-1} and the L_2 mode at around 686 cm^{-1},[69] which are displayed as vertical dashed lines in Fig. 9. Therefore, the 380–560 cm^{-1} region in the rotational power spectrum can be related to L_1 and the 600–1000 cm^{-1} region to L_2. Note that the power spectra do not contain intensity information. In the translational power spectrum of water, one can find a peak at around 294 cm^{-1} (label A in Fig. 9). Decomposing the translational power spectrum into *x*-, *y*-, and *z*-components, we note that this peak is missing in the *y*-direction, while it can be found in the *x*- and *z*-directions. As the *y*-axis (see Fig. 1) is normal to the H_2O/CO_2 interface, this peak likely corresponds to a translational motion of water, which is blocked in the *y*-direction due to the CO_2 layers adjacent to the water molecules.

For the layered H_2O–CO_2 ice, the H_2O bending mode appears as a combination of several peaks at around 1595–1645 cm^{-1} in the simulations. The patterns depend somewhat on temperature. The H_2O power spectra for the bending angle obtained for the 1st, 2nd, and 3rd layer H_2O molecules (not shown) clearly show one main band at around 1624 cm^{-1}, confirming that the IR peaks in the range from 1595–1645 cm^{-1} correspond to the water bending mode. More peaks appearing in the IR spectra in this region compared to a single main peak in the power spectra indicate that there may be some coupling of the bending motion with other modes. Furthermore, the bending mode in the power spectrum for the 1st layer water molecules appears at slightly lower wavenumber compared with the 2nd or 3rd layer water molecules, while the spectra from the 2nd and 3rd layer water molecules nearly coincide. The shift of the water bending mode to lower frequencies in a CO_2-rich environment is in agreement with frequency shifts observed for different compositions of mixed H_2O–CO_2 ices.[18]

The hydrogen atoms of the water molecules are equivalent on average in a bulk environment, and two OH stretchings are combined to form symmetric and antisymmetric stretching modes. However, for water molecules at an interface, the hydrogen atoms can experience different environments, depending on the orientation with respect to the interface. Hydrogen atoms involved in O–H bonds in the direction of the surface normal cannot form H-bonds (free O–H), while those parallel to the surface can participate in H-bonds to neighboring water molecules. To assess the difference between free and H-bonded OH-stretching vibrations in the first water layer from the interface, power spectra were computed for free and H-bonded O–H bonds in the first layer water molecules. For each type, five O–H bonds were randomly selected. The selected O–H groups are shown in the upper panel of Fig. 10, where the H atoms of free O–H are shown in green and those of H-bonded O–H in blue, respectively.

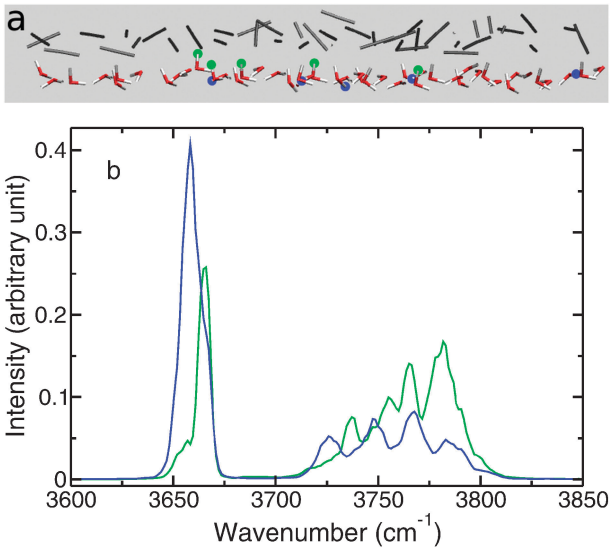

Fig. 10 (a) Selected atoms of free and H-bonded O–H groups for the calculation of the power spectra. The H atoms of free O–H are shown in green spheres and those of H-bonded O–H in blue spheres. The CO_2 molecules in the 1st layer are shown as gray linear bars above the water layer. (b) The power spectra of O–H stretching from two different types of O–H selected from the 1st-layer water molecules to estimate the difference in frequency. The power spectrum from free O–H is displayed in green and that from hydrogen-bonded O–H in blue.

For H-atoms involved in hydrogen bonds, the average H–O–H angle is $\sim$108.3°. Averaged power spectra are shown in the lower panel of Fig. 10. The spectral signatures extend over 150 cm^{-1} ranging approximately from 3650 to 3800 cm^{-1}, which compares with experimentally observed peaks at around 3200–3400 cm^{-1} obtained from sum frequency generation (SFG) spectroscopy at the water–air or water–lipid interface.[70] Two broad SFG peaks at around 3200–3400 cm^{-1} are interpreted as the OH-stretching vibration of strongly hydrogen-bonded water (3235 cm^{-1}) and weakly hydrogen-bonded water (3380 cm^{-1}), respectively.[70] The computed peaks for OH-stretching bands involved in H-bonds are redshifted compared to free OH stretches. The OH-stretching bands are redshifted further in the case of hexagonal ice, as can be observed in the experimental IR spectrum at $\sim$100 K, which shows a strong peak at $\sim$3220 cm^{-1} (ν_3) and a shoulder peak at $\sim$3085 cm^{-1} (ν_1).[66] The OH-stretching peaks are observed in the computed spectra at around 3658 cm^{-1} and 3782 cm^{-1} with the difference of 124 cm^{-1} for H_2O–CO_2 interface, while the experimental peaks are found at around 3235 cm^{-1} and 3380 cm^{-1} with the difference of 145 cm^{-1} for the water–air interface, as mentioned above.[70] The experimentally observed redshift of the OH-stretching mode in the condensed phase compared with the gas phase is known to be difficult to reproduce from simulations with existing water models.[56] This is also the case for the water model used in this work.

Rotational correlation times: to further investigate the possible difference in the motional freedom for molecules in different layers, the rotational correlation functions (RCFs) were computed. The data were fitted to an exponential function with a time constant τ_2, *i.e.*, $a\exp(-t/\tau_2) + c$. We obtained τ_2 values at 100, 150, and 200 K for CO_2, but only at 200 K for H_2O as water molecules did not show appreciable relaxation at lower temperatures. The fitting yields τ_2 = 57, 48, and 65 ps at 100 K, 8.4, 4.4, and 4.2 ps at 150 K, and 1.5, 1.6, and 1.8 ps at 200 K for CO_2 molecules in the 1st, 2nd, and 3rd layers from the interface, respectively. Thus, a pronounced temperature dependence is observed for the rotational correlation time.

The CO_2 reorientational correlation time was experimentally determined from measuring the ^{17}O longitudinal relaxation time $T_1(^{17}O)$ by NMR, under gaseous, liquid, and supercritical conditions at temperatures between 293 and 351 K over pressures ranging from 1 to 20 MPa.[51] The experimentally observed reorientation times were between 0.24 and 0.40 ps under these conditions. The extrapolation of the reorientation times from the simulations as a function of temperature to T = 300 K using an Arrhenius-like equation yields τ_2 = 0.59, 0.50, and 0.46 ps for the 1st, 2nd, and 3rd CO_2 layers, which compares quite favorably with the experimentally observed time scales. This is a further validation of the simulation strategy (parametrization and multipole moments) used in the present work.

For H_2O, four different τ_2 values were determined at 200 K, namely corresponding to $\boldsymbol{u}_{HH}$, $\boldsymbol{u}_{OH}$, $\boldsymbol{u}_{\mu}$, and $\boldsymbol{u}_{\perp}$, respectively, as described in the "Computational methods" section. The values of τ_2^{HH}, τ_2^{OH}, τ_2^{μ}, and $\tau_2^{\perp}$ are 3.9, 3.5, 2.9, and 3.9 ps for the 1st layer water molecules, 3.1, 2.7, 2.3, and 3.3 ps for the 2nd layer, and 2.5, 2.3, 1.9, and 2.7 ps for the 3rd layer.

For H_2O, the experimental values of τ_2^{HH} and τ_2^{OH} are 2.0 ps at 300 K,[50] which is smaller than our computed values at 200 K, as expected, since water molecules can rotate faster at higher temperatures. If we compare the characteristic rotational temperatures, $\Theta_{rot} = \hbar^2/2Ik_B$, where I is the moment of inertia, the value for CO_2 (0.561 K) is much smaller than those for H_2O (40.1, 20.9, and 13.4 K).[52] So we expect that H_2O would rotate much faster in the gas phase at a given temperature than CO_2, as one component of the rotational energy, $E_{rot} = I\omega^2/2$, should have the same value of $k_BT/2$, irrespective of the molecules or components, if the temperature is sufficiently higher than the characteristic rotational temperature. We note that τ_2 of H_2O is larger than that of CO_2 at the same temperature, *i.e.*, H_2O rotates slower than CO_2 on average, which reflects the extensive H-bond networks of water.

4 Conclusions

Atomistic molecular dynamics simulations were performed for layered mixed ices of water and carbon dioxide at temperatures relevant to interstellar and laboratory conditions using multipolar force fields to describe the electrostatic intermolecular interactions more accurately. From the simulations it was possible to analyze the structural and spectroscopic properties in more detail and relate spectroscopic features to variations in the local ice structure. The local environment affects the structural properties of each molecular species at different levels: in the mixed ice, the distribution of H_2O and CO_2 molecules differs from that in the gas or pure condensed phase. At the interface, templating effects exercised by the more strongly interacting component (water) on the more weakly interacting one (CO_2) are found. This change is gradual and more pronounced for CO_2. H_2O in contrast seems

to be far less affected by the proximity to the interface. Despite the lack of a pronounced structural change for different H_2O layers, the dynamics of H_2O is affected by the proximity to CO_2, as can be seen from the decrease in rotational correlation times with increasing distance from the interface. This decrease is observed for H_2O and CO_2, indicating that the rotation is hindered by the presence of the interface or the interface structure. From the simulations, the IR signatures from H_2O and CO_2 can be separately analyzed and it is found that the spectrum in the low-frequency region is dominated by the water molecules. Further, we obtained IR spectra from a single layer of a particular molecular species and showed that the spectra from different layers near the interface display different features. These features can be related to the change in molecular structure and molecular arrangements which depend on the local environment. For such assignments, power spectra can help to assist assignment of different features in the IR spectra, including translations, rotations, bending, and stretching motions. The spectroscopic changes are particularly pronounced in the far-IR region, which is directly related to the local structure and is currently being investigated using airborne experimental methods. In this spectral region, given spectroscopic features appear only in certain layers. For the higher-frequency regions, the environment-dependent change of spectral properties can be seen in band shifts and intensity modulations of various absorption bands, *e.g.* in the water O–H stretch region. Based on this layer-specific analysis of spectroscopic features we can predict the trends in line intensities and line shifts for different ice layer structures. Depending on the interface-to-bulk ratio of the ice, spectroscopic features and shifts observed in the layers near the interface will have variable contributions to the overall spectrum.

Acknowledgements

The authors gratefully acknowledge financial support from the Swiss National Science Foundation through grant 200021-117810.

References

1 L. J. Allamandola, M. P. Bernstein, S. A. Sandford and R. L. Walker, *Space Sci. Rev.*, 1999, **90**, 219–232.
2 R. L. Hudson, *J. Chem. Educ.*, 2006, **83**, 1611–1616.
3 M. H. Moore and R. L. Hudson, *Astron. Astrophys., Suppl. Ser.*, 1994, **103**, 45–56.
4 K. M. Ferrière, *Rev. Mod. Phys.*, 2001, **73**, 1031–1066.
5 *Origin and Evolution of Planetary and Satellite Atmospheres*, ed. S. K. Atreya, J. B. Pollack and M. S. Matthews, Univ. of Arizona Press, Tucson, 1989.
6 K. I. Öberg, H. J. Fraser, A. C. A. Boogert, S. E. Bisschop, G. W. Fuchs, E. W. van Dishoeck and H. Linnartz, *Astron. Astrophys.*, 2007, **462**, 1187–1198.
7 S. E. Bisschop, G. W. Fuchs, A. C. A. Boogert, E. F. van Dishoeck and H. Linnartz, *Astron. Astrophys.*, 2007, **470**, 749–759.
8 J. R. Brucato, G. A. Baratta and G. Strazzulla, *Astron. Astrophys.*, 2006, **455**, 395–399.
9 P. Vernazza, T. Mothé-Diniz, M. A. Barucci, M. Birlan, J. M. Carvano, G. Strazzulla, M. Fulchignoni and A. Migliorini, *Astron. Astrophys.*, 2005, **436**, 1113–1121.
10 G. A. Baratta, M. E. Palumbo and G. Strazzulla, *Astron. Astrophys.*, 2000, **357**, 1045–1050.
11 J. E. Chiar, Y. J. Pendleton, L. J. Allamandola, A. C. A. Boogert, K. Ennico, T. P. Greene, T. R. Geballe, J. V. Keane, C. J. Lada, R. E. Mason, T. L. Roellig, S. A. Sandford, A. G. G. M. Tielens, M. W. Werner, D. C. B. Whittet, L. Decin and K. Eriksson, *Astrophys. J.*, 2011, **731**, 9.
12 R. M. Mastrapa, S. A. Sandford, T. L. Roush, D. P. Cruikshank and C. M. Dalle Ore, *Astrophys. J.*, 2009, **701**, 1347–1356.
13 M. P. Bernstein, S. A. Sandford, A. L. Mattioda and L. J. Allamandola, *Astrophys. J.*, 2007, **664**, 1264–1272.
14 J. A. Graham and W. P. Chen, *Astron. J.*, 1991, **102**, 1405–1408.
15 J. A. Graham, *Astrophys. J.*, 1998, **492**, 213–218.
16 L. J. Allamandola, S. A. Sandford, A. G. G. M. Tielens and T. M. Herbst, *Astrophys. J.*, 1992, **399**, 134–146.
17 R. W. Henning, A. J. Schultz, V. Thieu and Y. Halpern, *J. Phys. Chem. A*, 2000, **104**, 5066–5071.
18 N. Plattner, M. W. Lee and M. Meuwly, *Faraday Discuss.*, 2010, **147**, 217–230.
19 R. D. Gehrz, E. E. Becklin, J. de Buizer, T. Herter, L. D. Keller, A. Krabbe, P. M. Marcum, T. L. Roellig, G. H. L. Sandell, P. Temi, W. D. Vacca, E. T. Young and H. Zinnecker, *Adv. Space Res.*, 2011, **48**, 1004–1016.
20 A. M. Cook, D. C. B. Whittet, S. S. Shenoy, P. A. Gerakines, D. W. White and J. E. Chiar, *Astrophys. J.*, 2011, **730**, 124.
21 A. A. Schegerer and S. Wolf, *Astron. Astrophys.*, 2010, **517**, A87.
22 Y. Oba, N. Miyauchi, H. Hidaka, T. Chigai, N. Watanabe and A. Kouchi, *Astrophys. J.*, 2009, **701**, 464–470.
23 B. Maté, O. Gálvez, V. J. Herrero and R. Escribano, *Astrophys. J.*, 2009, **690**, 486–495.
24 M. E. Palumbo and G. Strazzulla, *Astron. Astrophys.*, 1993, **269**, 568–580.
25 S. A. Sandford, L. J. Allamandola, A. G. G. M. Tielens and G. J. Valero, *Astrophys. J.*, 1988, **329**, 498–510.
26 B. Maté, O. Gálvez, B. Martín-Llorente, M. A. Moreno, V. J. Herrero, R. Escribano and E. Artacho, *J. Phys. Chem. A*, 2008, **112**, 457–465.
27 R. J. Phillips, B. J. Davis, K. L. Tanaka, S. Byrne, M. T. Mellon, N. E. Putzig, R. M. Haberle, M. A. Kahre, B. A. Campbell, L. M. Carter, I. B. Smith, J. W. Holt, S. E. Smrekar, D. C. Nunes, J. J. Plaut, A. F. Egan, T. N. Titus and R. Seu, *Science*, 2011, **332**, 838–841.
28 M. P. Bernstein, D. P. Cruikshank and S. A. Sandford, *Icarus*, 2005, **179**, 527–534.
29 D. W. White, P. A. Gerakines, A. M. Cook and D. C. B. Whittet, *Astrophys. J.*, 2009, **180**, 182–191.
30 B. Rowland and J. P. Devlin, *J. Chem. Phys.*, 1991, **94**, 812–813.
31 B. Rowland, M. Fisher and J. P. Devlin, *J. Chem. Phys.*, 1991, **95**, 1378–1384.
32 J. P. Devlin, *J. Phys. Chem.*, 1992, **96**, 6185–6188.
33 B. Rowland, M. Fisher and J. P. Devlin, *J. Phys. Chem.*, 1993, **97**, 2485–2487.
34 D. R. Nutt and M. Meuwly, *Biophys. J.*, 2003, **85**, 3612–3623.
35 N. Plattner, T. Bandi, J. D. Doll, D. L. Freeman and M. Meuwly, *Mol. Phys.*, 2008, **106**, 1675–1684.
36 N. Plattner and M. Meuwly, *ChemPhysChem*, 2008, **9**, 1271–1277.
37 N. Plattner and M. Meuwly, *Biophys. J.*, 2008, **94**, 2505–2515.
38 B. R. Brooks, R. E. Bruccoleri, B. D. Olafson, D. J. States, S. Swaminathan and M. Karplus, *J. Comput. Chem.*, 1983, **4**, 187–217.
39 S. Nosé, *J. Chem. Phys.*, 1984, **81**, 511–519.
40 W. G. Hoover, *Phys. Rev. A*, 1985, **31**, 1695–1697.
41 W. H. Keesom and J. W. L. Köhler, *Physica*, 1934, **1**, 167–174.
42 N. Kumagai, K. Kawamura and T. Yokokawa, *Mol. Simul.*, 1994, **12**, 177–186.
43 C. J. Burnham, J. C. Li and M. Leslie, *J. Phys. Chem. B*, 1997, **101**, 6192–6195.
44 M. W. Lee and M. Meuwly, *J. Phys. Chem. A*, 2011, **115**, 5053–5061.
45 R. Lemus, *J. Mol. Spectrosc.*, 2004, **225**, 73–92.
46 *CCCBDB*, http://cccbdb.nist.gov [Online; accessed 29 September 2011].
47 M. J. Frisch, G. W. Trucks, H. B. Schlegel, G. E. Scuseria, M. A. Robb, J. R. Cheeseman, J. A. Montgomery Jr., T. Vreven, K. N. Kudin, J. C. Burant, J. M. Millam, S. S. Iyengar, J. Tomasi, V. Barone, B. Mennucci, M. Cossi, G. Scalmani, N. Rega, G. A. Petersson, H. Nakatsuji, M. Hada, M. Ehara, K. Toyota, R. Fukuda, J. Hasegawa, M. Ishida, T. Nakajima, Y. Honda, O. Kitao, H. Nakai, M. Klene, X. Li,

J. E. Knox, H. P. Hratchian, J. B. Cross, C. Adamo, J. Jaramillo, R. Gomperts, R. E. Stratmann, O. Yazyev, A. J. Austin, R. Cammi, C. Pomelli, J. W. Ochterski, P. Y. Ayala, K. Morokuma, G. A. Voth, P. Salvador, J. J. Dannenberg, V. G. Zakrzewski, S. Dapprich, A. D. Daniels, M. C. Strain, O. Farkas, D. K. Malick, A. D. Rabuck, K. Raghavachari, J. B. Foresman, J. V. Ortiz, Q. Cui, A. G. Baboul, S. Clifford, J. Cioslowski, B. B. Stefanov, G. Liu, A. Liashenko, P. Piskorz, I. Komaromi, R. L. Martin, D. J. Fox, T. Keith, M. A. Al-Laham, C. Y. Peng, A. Nanayakkara, M. Challacombe, P. M. W. Gill, B. Johnson, W. Chen, M. W. Wong, C. Gonzalez and J. A. Pople, *Gaussian 03, Revision B.01*, Pittsburgh, PA, 2003.

48 M. P. Allen and D. J. Tildesley, *Computer Simulation of Liquids*, Oxford University Press, New York, 1987.

49 J. E. Adams and A. Siavosh-Haghighi, *J. Phys. Chem. B*, 2002, **106**, 7973–7980.

50 D. van der Spoel, P. J. van Maaren and H. J. C. Berendsen, *J. Chem. Phys.*, 1998, **108**, 10220–10230.

51 T. Umecky, M. Kanakubo and Y. Ikushima, *J. Phys. Chem. B*, 2003, **107**, 12003–12008.

52 D. A. McQuarrie, *Statistical Mechanics*, Harper & Row, New York, 1976.

53 F. Li and J. L. Skinner, *J. Chem. Phys.*, 2010, **133**, 244504.

54 G. Herzberg, *Molecular Spectra and Molecular Structure; II. Infrared and Raman Spectra of Polyatomic Molecules*, D. Van Nostrand Company, New York, 1945.

55 G. E. Ewing, *J. Phys. Chem. B*, 2004, **108**, 15953–15961.

56 C. J. Burnham, G. F. Reiter, J. Mayers, T. Abdul-Redah, H. Reichert and H. Dosch, *Phys. Chem. Chem. Phys.*, 2006, **8**, 3966–3977.

57 Y. Maréchal, *J. Mol. Struct.*, 2011, **1004**, 146–155.

58 W. Chen, M. Sharma, R. Resta, G. Galli and R. Car, *Phys. Rev. B: Condens. Matter Mater. Phys.*, 2008, **77**, 245114.

59 S. Lammers and M. Meuwly, *J. Phys. Chem. A*, 2007, **111**, 1638–1647.

60 R. L. Hudson and M. H. Moore, *J. Phys. Chem.*, 1992, **96**, 6500–6504.

61 M. H. Moore and R. L. Hudson, *Astrophys. J.*, 1992, **401**, 353–360.

62 S. Krishnamurthy, R. Bansil and J. Wiafe-Akenten, *J. Chem. Phys.*, 1983, **79**, 5863–5870.

63 D. Tazawa, M. Kobayashi and S. Endo, Abstracts of the meeting of the Physical Society of Japan. Annual meeting, 1995, **50**, 89.

64 V. F. Petrenko and R. W. Whitworth, *Physics of Ice*, Oxford University Press, New York, 1999.

65 J. Li, J. D. Londono, D. K. Ross, J. L. Finney, J. Tomkinson and W. F. Sherman, *J. Chem. Phys.*, 1991, **94**, 6770–6775.

66 J. E. Bertie, H. J. Labbé and E. Whalley, *J. Chem. Phys.*, 1969, **50**, 4501–4520.

67 A. Anderson and S. H. Walmsley, *Mol. Phys.*, 1964, **7**, 583–586.

68 Y. R. Shen, *Nature*, 1989, **337**, 519–525.

69 H. R. Zelsmann, *J. Mol. Struct.*, 1995, **350**, 95–114.

70 A. Ghosh, M. Smits, M. Sovago, J. Bredenbeck, M. Müller and M. Bonn, *Chem. Phys.*, 2008, **350**, 23–30.

